JATIS Journal of Astronomical Telescopes, Instruments, and Systems

RESEARCH PAPER

New extreme ultraviolet transmission measurements of two thin-film filters for imaging of plasmaspheric cold ions

Philippa Molyneux,[a] **Todd Veach**,[a,b] **Michael Davis**,[a] **Gregory Fletcher**,[a] **and Jerry Goldstein**[a,b,*]

[a]Southwest Research Institute, San Antonio, Texas, United States
[b]University of Texas San Antonio, San Antonio, Texas, United States

ABSTRACT. We present extreme ultraviolet (EUV) transmission measurements of two thin-film filters designed to obtain improved images of plasmaspheric He^+, and the first global images of O^+/O^{++} in the dense oxygen torus. Compared to previous He^+ 30.4 nm imaging that used an Al filter, we show that a combined Al+C filter achieves superior rejection of 58.4 nm background from neutral helium (He I). We show that an indium filter provides both the required transmission at 83.4 nm and adequate rejection of brighter He I (58.4 nm) and H I (121.6 nm) background emissions. We find that the In transmission at 58.4 nm is a factor of ~16 lower than predicted based on optical constants that rely on interpolations at $\lambda < 68$ nm. We show that the observed lower 58.4 nm transmission is consistent with alternative optical constants derived from previous lab measurements.

Keywords: extreme ultraviolet; extreme ultraviolet; thin-film filters

Paper 23077G received Jul. 17, 2023; revised Jan. 31, 2024; accepted Feb. 7, 2024; published Mar. 4, 2024.

1 Introduction

The extreme ultraviolet (EUV) spectral regime (10 to 121 nm) is well-suited for remote observations of the Earth's plasmasphere—the population of cold, dense plasma that extends several Earth radii (R_E) from the planet. Important plasmaspheric ion species including helium (He^+) and oxygen (O^+ and O^{++}) have bright emission lines in this wavelength range.[1,2] The EUV imager on NASA's IMAGE mission first obtained routine global images of 30.4 nm light resonantly scattered by plasmaspheric He^+ ions, allowing the density and distribution of the plasma to be monitored at 10-min time resolution.[3] The IMAGE EUV imager's three-camera design was updated to a single camera with a wider field of view (FOV); this augmented design is referred to as D13.[4] The D13 camera design implemented small modifications to IMAGE EUV to improve the FOV, resolution, and sensitivity to achieve 1-min resolution, which could help answer a number of outstanding science questions such as how the plasmasphere is eroded and redistributed during geomagnetic disturbances.[2] One of the D13 design modifications is the addition of a thin carbon layer to the aluminum filter at the IMAGE EUV entrance filter, leading to a predicted factor-of-five reduction in transmittance of the neutral helium emission at 58.4 nm—reducing a significant background signal for 30.4 nm images. The technique of adding C layers to Al to attenuate longer-wavelength light was used previously for the filters on the EUVE mission.[5]

*Address all correspondence to J. Goldstein, jgoldstein@swri.org

The D13 camera design was further optimized/reconfigured to image 83.4 nm light; this updated design is referred to as G18.[6] The G18 camera uses the identical optical design as D13, but selects alternate filter and mirror coating materials in order to image 83.4 nm emissions from O^+ and O^{++} within the dense oxygen torus. The dense torus is a region of enhanced oxygen ion densities in the outer plasmasphere that has been detected by in situ instruments during or after storms, but has not yet been imaged.[7–10] A wide-field imager capable of detecting light at 83.4 nm would achieve the first global view of the oxygen torus, addressing basic questions about its distribution and formation.[6]

One of the key challenges of 83.4 nm imaging is that few filter materials transmit well at that wavelength. One identified option for dense torus imaging is indium,[6] owing to its relatively high transmittance at 83.4 nm and good rejection of Lyman alpha at 121.6 nm. However, previous transmission measurements of thin film indium filters have found large variance among measurements of the absolute transmission around 75 to 90 nm, although the shape of the transmission versus wavelength curve is generally consistent with the predictions.[11–13] The exception to this shape concordance is an apparent discrepancy between the previously measured transmission at 58.4 nm and the modeled transmission curve based on optical constants obtained via synthesis of experimental data and theoretical photoabsorption calculations.[14] That is, the measured relative transmission of 58.4 nm (compared to that at 83.4 nm) is lower than predicted.[13,15] If this apparent transmission minimum at 58.4 nm is real, it further increases the attractiveness of indium as a filter material for imaging of the 83.4 nm O^+/O^{++} plasmasphere emissions, since bright helium emissions at 58.4 nm are expected to contribute significantly to the background in such images.

In this paper, we present new transmission measurements of thin film Al/C and In filters, demonstrating that they meet the requirements of both transmission of on-band photons, and filtering of off-band photons, for imaging plasmaspheric He^+ and O^+/O^{++}, respectively.

2 Filter Performance Requirements

When assessing the performance of the thin film filters, we assume they are used in the D13[4] or G18[6] optimized version of the IMAGE EUV optical design (Fig. 1). Light falling within the 40 deg FOV passes through an annular filter onto the spherical primary mirror, and is reflected toward a spherically slumped microchannel plate (MCP) detector. We assume that the imager targeting 30.4 nm (hereinafter EUV-He) uses the D13 periodic Mg/SiC multilayer mirror coating,[4] and the 83.4 nm imager (EUV-O) uses the G18 aperiodic Al-Mg/SiC multilayer coating.[6] MCP detectors are often coated with a photocathode material to increase the quantum efficiency in the targeted spectral region. For example, the MCP detector for Juno UVS (cf. Sec. 3) is optimized for the far ultraviolet through the use of a CsI photocathode.[16] In contrast, IMAGE EUV used a bare MCP detector for reduced Lyman alpha sensitivity with good EUV response near 30.4 nm.[3] For our EUV filter design, we assume both EUV-He and EUV-O use bare MCPs, as baselined for the G18 imager.[6]

To determine the required thicknesses of the filters to be tested, we considered the instrument sensitivity, S_λ, defined as the expected count rate per resolution element for a source emitting at wavelength λ with intensity 1 R (where $1\,\mathrm{R} = 10^6/4\pi$ photons $\mathrm{cm}^{-2}\,\mathrm{s}^{-1}\,\mathrm{sr}^{-1}$). The EUV sensitivity is estimated to be[3]

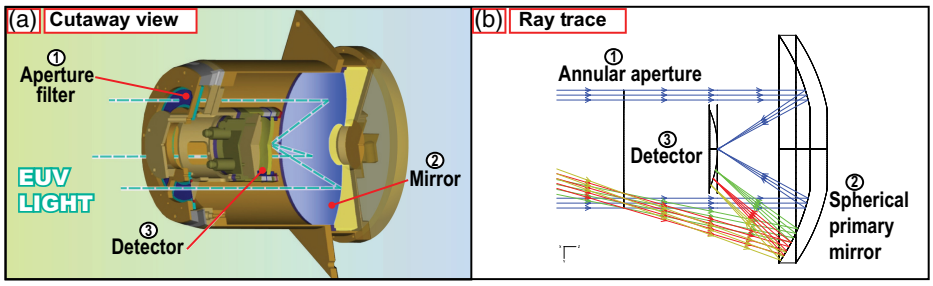

Fig. 1 D13 and G18 optical design. D13/G18 are improved/updated versions of IMAGE EUV; see text. (a) Cutaway view. (b) Ray trace diagram. EUV light within ±20 deg of the optical axis transits the annular filter and is focused by the spherical mirror onto a spherically slumped MCP detector.

Table 1 Estimated sensitivity of EUV-He (30.4 nm) and EUV-O (83.4 nm) imagers, using theoretical transmissions.

Imager	Filter	Wavelength λ (nm)	Detect- or efficiency ε_λ	Theoretical Filter transmission[a] τ_λ	Mirror reflectivity[b] ρ_λ	Sensitivity S_λ $(\mathrm{R\,s\,pix})^{-1}$	Model-expected background (BG) rejection $S_\lambda \div S_{\mathrm{target}}$	Required BG rejection
EUV-He	Al (244 nm) + C (29 nm)	58.4	0.12	0.0036	0.01	7.0×10^{-4}	5.3×10^{-4}	4×10^{-3}
		30.4	0.2	0.14	0.32	1.34	—	—
		121.6	0.01	1.0×10^{-13}	0.05	7.7×10^{-15}	5.8×10^{-15}	7×10^{-6}
EUV-O	In (303 nm)	58.4	0.12	1.3×10^{-3}	0.004	7.7×10^{-5}	2.0×10^{-4}	1×10^{-3}
		83.4	0.085	0.12	0.32	0.38	—	—
		121.6	0.01	7.8×10^{-8}	0.60	1.2×10^{-7}	3.2×10^{-7}	1×10^{-6}

[a]Filter transmission values: from UV optical constants.[14]
[b]Mirror reflectivity values: from D13[4] for EUV-He and G18[6] for EUV-O.

$$S_\lambda = A\omega\varepsilon_\lambda\tau_\lambda\rho_\lambda 10^6/4\pi, \tag{1}$$

where A is the open aperture area, ω is the angular size of a resolution element, ε_λ is the detector quantum efficiency, τ_λ is the filter transmission, and ρ_λ is the mirror reflectance. For A and ω we use the D13 values of 30 cm^2 and $(0.45\ \mathrm{deg})^2$, respectively.[4] We use ε_λ values for bare borosilicate MCP detectors[17] and mirror reflectivity (ρ_λ) data from D13[4] and G18[6] for EUV-He and EUV-O, respectively. We calculate the predicted transmission (τ_λ) of Al/C and In filters from their UV optical constants,[14] adjusting the filter thicknesses to optimize the transmission at the target wavelength (30.4 or 83.4 nm), while achieving the required rejection of the background 58.4 and 121.6 nm emissions.

The background rejection factors (defined as $S_\lambda \div S_{30.4}$) required for the EUV-He 30.4 nm imager are $(4\times10^{-3}, 7\times10^{-6})$ for (58.4, 121.6) nm. For this study, we chose to test an EUV-He filter consisting of a 244 nm Al film combined with a 29 nm thin film of carbon, which is expected to achieve these requirements with considerable margin (see Table 1).

Plasmaspheric oxygen imaging requires background rejection factors (defined as $S_\lambda \div S_{83.4}$) better than $(10^{-3}, 10^{-6})$ for (58.4, 121.6) nm, which may be achieved using an indium filter with thickness in the range 270 to 330 nm.[6] The expected performance of a 303.2 nm indium filter is shown in Table 1. This initial estimate of optimal filter thickness (OFT) of 303.2 nm is chosen based on theoretically-predicted indium transmission; later in Sec. 5.1, we use filter transmission measurements to refine the OFT estimate. The EUV-O mirror coating has a high reflectivity (0.6) at 121.6 nm, making the filter performance particularly critical at this wavelength. To minimize the effects of any pinholes due to micrometeoroids hitting the filter in flight, we suggest the use of two half-thickness filters rather than a single filter. The probability of dust impact damage leading to significant 121.6 nm light leaks is thereby reduced since particles must impact with the correct velocity to penetrate both filters (faster particles vaporize on the front filter[18]) and at a small enough angle that on-axis light encounters both pinholes. The two-layer filter as a pinhole mitigation technique was implemented for the Multi-Spectral Solar Telescope Array.[19] For EUV-O, we therefore chose to test half-thickness (303.2 nm ÷ 2) indium filters, i.e., 151.6 nm (±5%).

3 Filter Transmission Measurements

We measured the EUV transmission of Luxel Al/C and In thin film filters with thicknesses of (a) 244 nm (Al) + 29 nm (C) for EUV-He, and (b) 152 nm (In) for EUV-O. The thickness tolerance (as quoted by Luxel) on each material was ±5% and each filter was supported by a 70 line-per-inch nickel mesh, providing an open area fraction of 82%. Note that for the Al/C filter, a single C layer was added to the Al, rather than a C/Al/C configuration. (See discussion of oxide layer, Sec. 4.1.)

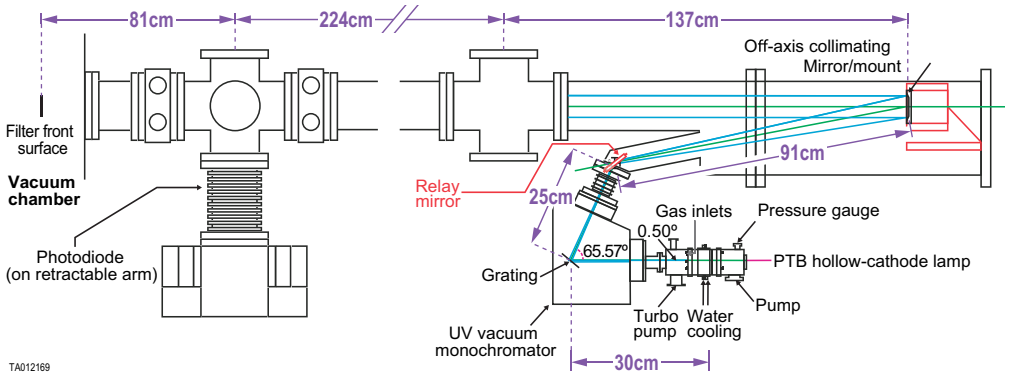

Fig. 2 The SwRI UV-RCF test facility.

All measurements were performed in the Ultraviolet Radiometric Calibration Facility (UV-RCF)[20] at the Southwest Research Institute (SwRI) in San Antonio, TX. The SwRI UV-RCF (Fig. 2) consists of a 0.75-m diameter, 2-m long vacuum chamber connected to an evacuated beam line. A collimated monochromatic beam of light is provided by a 10-cm diameter off-axis parabolic collimator mirror fed by a differentially-pumped hollow-cathode UV light source and a UV vacuum monochromator (Acton Research Corporation VM-502).[21] The beam flux is monitored with a windowless NIST (National Institute of Standards and Technology) calibrated photodiode (International Radiation Detectors, model AXUV-100G), mounted on a motorized arm to allow movement in and out of the beam as required. Four different gases are available for use in the lamp: argon (Ar), neon (Ne), carbon dioxide (CO_2), and a 95% helium +5% hydrogen mix (H_2/He).

For each test, the filter being measured was mounted in the UV-RCF vacuum chamber facing the beam. A flight spare Juno UVS MCP detector[16] was placed behind the filter to detect photons passing through the filter, and Al foil was fitted around the filter mount to reduce scattered light. Exposure times are given in Table 2. In principle, the filter transmission can be determined by comparing the photon flux observed by the Juno UVS detector to the flux measured by the beam monitoring NIST-calibrated photodiode. However, this approach requires reliable knowledge of the EUV quantum efficiencies (QEs) of both the MCP detector and the photodiode. Furthermore, input beam levels that provide sufficient signal-to-noise on the photodiode will saturate the MCP detector readout, making cross-calibration without a transfer standard difficult. The Juno UVS

Table 2 Exposure times for measurements with Al/C (EUV-He) and In (EUV-O) filters.

	Exposure times	
Emission line wavelength (nm)	Al/C filter (s)	In filter (s)
30.4	300	—
46.1	60	150
58.4	300	300
74.0	300	300
83.0	300	—
83.4	—	300
93.0	—	300
105.0	—	300
121.6	60	60

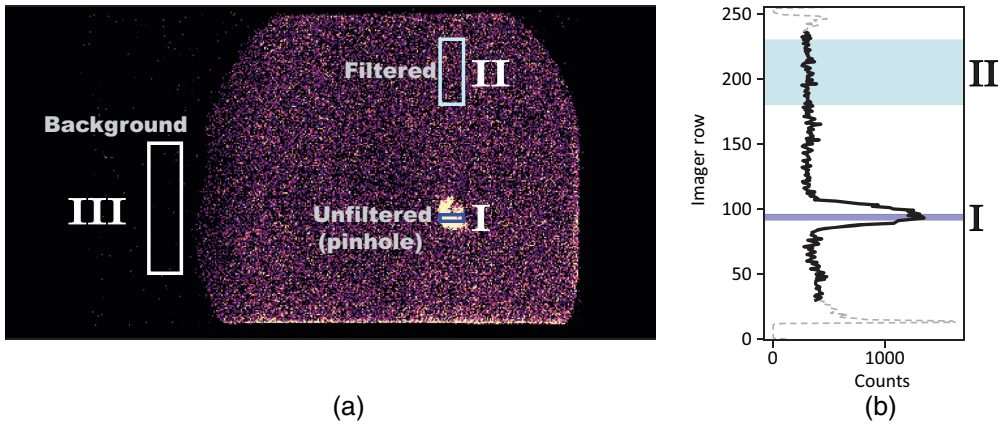

Fig. 3 Example image using Al/C filter. (a) Image obtained through the Al/C filter at 30.4 nm. Labeled rectangles indicate the areas used to measure: the unfiltered count rate (I), the filtered count rate (II), and the background count rate (III). (b) Counts per image row in the portion of the image spanning the width of rectangles I and II.

MCP has only been calibrated for $\lambda > 115$ nm. Rather than attempting to extrapolate the detector QE curve to our wavelength range, we made a pinhole in each filter that would allow us to compare directly the filtered and unfiltered regions of the images obtained by the detector. Since the QE is expected to remain approximately constant versus detector position for any given wavelength, the estimated filter transmission is simply the ratio of the filtered and unfiltered count rates per unit area. An example image obtained through the Al/C filter at 30.4 nm is shown in Fig. 3, with regions used to measure filtered, unfiltered, and background count rates indicated by the colored rectangles. We used the pinhole method rather than a simpler "filter in, filter out" approach (i.e., moving the filter in and out of the beam via a motorized stage) for two reasons. (1) We were concerned that exposing large regions of the detector to some of the brighter unfiltered emissions (e.g., Lyman-α) could produce excessively high global count rates, which (b) could cause gain sag and dropped counts that degrade the reliability of the comparison with filtered images, and (a) might potentially damage the MCPs. (2) Installation of a vacuum-compatible motion stage was not practical within this project's modest budget and schedule.

The monochromator physically prevents undesired diffraction orders from reaching the collimator, unless there happens to be an order corresponding to an integer divisor of the selected wavelength. We chose not to add an additional bandpass filter to the system, because the uncertainty of that added filter's transmission would add significantly to that of our measurement, and the added filter would also reduce throughput. We are confident that no second-order emissions affect our hydrogen/helium and CO_2 measurements because published EUV spectra show no lines that could contribute in the second order.[22,23] We measured the second-order Lyman-α and found the flux was reduced by a factor of about 12. Any higher orders would be reduced by even larger factors, and we would expect negligible impact on the measured fluxes. For Ne and Ar, we are less confident about possible higher-order contamination since fewer published spectra are available. Spectra for Ar/H_2 and Ne/H_2 mixtures within 25 to 50 nm[23] do not permit assessment of the relative first- and second-order intensities, and it is unclear if these published data are applicable to spectra of pure Ar and Ne. If the filter transmission at the second-order wavelength is significantly higher than at the first-order wavelength, second-order contamination can lead to overestimation of the transmission at the primary wavelength. This situation does not occur for any of the Indium Ar/Ne wavelengths. For the Al/C 83.0 and 74.0 nm measurements, the second-order transmissions do exceed those of the primary wavelength, and consequently, these measured transmissions might be overestimated. Quantifying the uncertainty associated with this possible overestimation requires reliable values of detector quantum efficiency and intensity at the second-order emission wavelengths, which should be pursued in future work.

For most measurements, we used a slit width of 325 μm to maximize the photon flux (and the SNR). The one exception was a narrowed, 100-μm slit width used for the 46.1 nm image through the Al/C filter, implemented to mitigate the risk of excessive counts to the detector from

Table 3 Measured transmission values of Al/C (EUV-He) and In (EUV-O) filters.

Emission line wavelength (nm)	Gas	Al/C transmission (%)	In transmission (%)
30.4	H/He	23.47 ± 5.17	—
46.1	Ne	2.94 ± 0.83	0.44 ± 0.13
58.4	H/He	0.47 ± 0.14	0.19 ± 0.07
74.0	Ne	0.69 ± 0.20	2.99 ± 0.85
83.0	Ar	0.15 ± 0.05	—
83.4	CO_2	—	28.17 ± 7.52
93.0	Ar	—	14.83 ± 4.20
105.0	Ar	—	5.74 ± 1.63
121.6	H/He	$\leq 2.72 \times 10^{-5}$	0.032 ± 0.011

the combination of the bright emission and the relatively high transmission of the filter at that wavelength. For reference, the total count rate in that 46.1 nm image was ~13 kHz with 100-μm slit width, quite comparable to the ~1.1 kHz count rate for the 58.4 nm image using a 325-μm slit (325% wider) width. The monochromator full-width dispersion is (1.3 nm, 0.4 nm) for a $(325, 100)$ μm slit. Most lines in the emission spectra of the gases used are separated by much larger wavelength distances. The presence of close multiplets (i.e., multiple lines passing through the slit in a single image) could add uncertainty to the measurement if the multiplet spans a wavelength range where there is a very sharp change in the transmission of the filter. Most of the argon and neon emissions we used are close multiplets, but they only overlap with a steep slope in transmission for the In filter at 74 nm. If the brighter 73.6 nm dominates over the 74.4 nm emission, the measured transmission curve might require a very minor adjustment; 74 nm is not a critical wavelength for our EUV-O imager.

We measured filter transmissions at emission line wavelengths between 30.4 nm and 121.6 nm, as listed in Table 3. Images similar to that of Fig. 3(a) were obtained for each filter at the wavelengths indicated. When the lamp was used with either the H_2/He mix or CO_2, excess scattered background was sometimes seen by the detector due to particularly strong emissions of neutral hydrogen (121.6 nm) and neutral oxygen (130.4 nm), from excited gas downstream of the monochromator. We therefore obtained background images at two wavelengths where no emission lines were expected, such that all signal detected in the image may be assumed to originate from glowing residual gases within the test system. The two wavelengths selected for background images are:

1. **35 nm**. We used the NIST Atomic Spectra Database[24,25] to identify and select the EUV wavelength of 35 nm for our background image with no expected H or He emission. The 35 nm background image was subtracted from images using the H_2/He gas.
2. **78 nm**. We obtained CO_2 background images at 78 nm, because although the full EUV spectrum of CO_2 contains many emission lines, the ~72 to 80 nm range is expected to be free of emission lines from CO_2.[22] The 78 nm background image was subtracted from images using CO_2.

Ne and Ar gas measurements exhibited no significant excess scattered background. Future calibration of a flight instrument might include an additional filter or grating to attenuate scattered light. As noted above, for our measurement we chose not to include this extra filter, to avoid added uncertainty and reduced throughput.

Extended use of CO_2 can cause buildup of UV-absorbing contaminants on surfaces within the UV-RCF system, due to reactions between the dissociation products of the gas and any residual atmospheric gases such as H_2O. To minimize the likelihood of contamination, we used CO_2 only to determine the In transmission for the EUV-O target 83.4 nm O^+/O^{++} emission.

Since 83.4 nm is a less important wavelength for the Al/C filter, we instead obtained images of faint neutral Ar emissions at 83.0 nm. The nominal monochromator dispersion (for slit width 325 μm) of 1.3 nm (full width) includes four Ar lines: (82.5, 82.6, 83.4, 83.5) nm (according to the NIST database). We consider these measurements less reliable than the equivalent CO_2 measurements, since the NIST database also lists argon ion emissions in the 40–42 nm range that may contribute to the 83.4 nm signal to second order.

We chose to use CO_2 to make 83.4 nm light for the In filter transmission measurement. Based on the theoretical In curve's shape near 83.4 nm (Sec. 4.2), one would expect a very similar In filter measurement at 83.0 nm using Ar. Our In measurement did not use Ar 83.0 nm light to avoid the contaminant buildup, because the Ar 83.0 nm emission may include second-order light contamination from possible Ar ion emissions in the 40 to 42 nm range that we are currently unable to characterize. Neither the Juno detector nor the beam monitoring photodiode are properly calibrated at these wavelengths. The CO_2 is therefore more reliable for the In filter measurement. Based on published EUV CO_2 spectra,[22] we are confident there is minimal second-order 40 to 42 nm contamination when using CO_2. We were unable to find equivalent published Ar spectra. Before future calibration of a flight instrument, we intend to characterize the full EUV argon spectrum to determine whether the neutral Ar emissions may be reliably used instead of CO_2.

General contamination mitigation strategies for the Al/C and In filters were employed as follows. The filters were never exposed to unfiltered air. They were removed from their shipping containers in a class 10,000 (ISO7) clean tent by personnel wearing full cleanroom suits and were never handled with bare hands or without face masks. When not being tested, the filters were stored in a dry nitrogen purge cabinet inside the clean tent. The purge cabinet was next to the UV test chamber, minimizing any time out of the nitrogen purge during the experimental setup. The test chamber was kept at ultrahigh vacuum ($\sim 10^{-6}$ Torr) except when changing the experiment configuration, at which time it was backfilled with nitrogen. For flight instrumentation, we further reduce the risk of contamination by storing filters and other optics in vacuum chambers. We are not currently able to quantify directly any contamination present; however, if we notice a degradation of filter performance during repeat tests, we can make use of plasma cleaning facilities similar to those demonstrated by previous work to improve EUV transmission by 50% to 500%.[26]

4 Results

The measured EUV transmission values for the two filters are given in Table 3 and described in the following subsections. For most wavelengths, measurements have sufficiently high count rates that counting statistical uncertainties only contribute a few percent (at most) to the total uncertainty estimates, and the largest source of error is spatial nonuniformity of the beam. (The beam was temporally stable within 2% after a warm-up period of 10 to 15 min.) We estimated the magnitude of the beam spatial variation as follows. We obtained an unfiltered image of the beam (i.e., with no Al/C or In filter, and split the image into 10 regions distributed evenly across the full width of the beam. From each region, we extracted vertical beam profiles similar to Fig. 3(b), and calculated the mean and standard deviation of the count rate in each profile, excluding the edge regions indicated by the dashed lines in Fig. 3(b), where an artificially increased count rate is caused by pile-up effects typical of MCP detectors.[16] The measured standard deviations varied from 12% to 27% of the mean flux in each image slice, with an average standard deviation of 19%, which we rounded up to 20% for our uncertainty estimates. We therefore calculated most transmission uncertainty values assuming a 20% variation in beam flux. We assume this 20% uncertainty in both the filtered and unfiltered count rates, and then combined the two in quadrature to yield error bars of about 28%. These 28% error bars were applied to most wavelengths, except for Al/C transmission uncertainty at 30.4 nm that was calculated from Poisson statistical uncertainty of the observed count rates, and Al/C transmission at 121.6 nm whose measurement is an upper-limit estimate, as described in Sec. 4.1. As noted above, for measurements away from 30.4 nm (with sufficiently high count rates), counting statistics was not a dominant source of error.

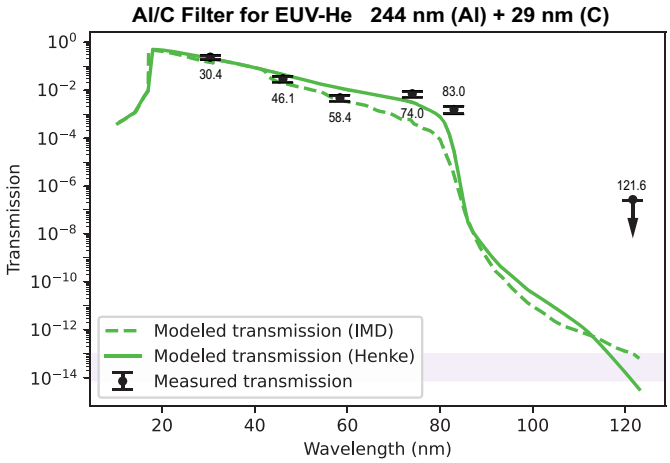

Fig. 4 EUV-He filter transmission. Measured Al/C filter transmission, compared to modeled transmission using two different sets of optical constants. Note: bandpass purity is ≤1.3 nm (based on monochromator dispersion; cf. Sec. 3). Horizontal extent of error bars in plot is graphically arbitrary.

4.1 Al/C Filter Transmission

The measured Al/C transmission values are listed in Table 3 and plotted in Fig. 4. Also plotted are two theoretical transmission curves: one ("Henke") based on the atomic form factors for Al and C,[14] and the other modeled using the IMD software package,[27] which includes compilations of optical constants of materials commonly used for optical coatings and filters. Note that our models do not explicitly include the oxide layer that is inevitably present on Al films exposed to air, but IMD uses optical constants from laboratory measurements where available. The presence of the oxide layer in these laboratory measurements may explain why the IMD model generally predicts lower transmission than the Henke model. Modeling the oxide layer and comparing our current results to a C/Al/C filter are topics for future work.

The measured transmission values generally follow the decreasing trend of the models between 30.4 and 83.4 nm, although no single model is consistent (within errors) with all of the data points. The measurements at 30.4 nm and 58.4 nm agree well (within one error bar) with the Henke or IMD models, respectively. Slightly worse agreement (within two error bars) with the Henke or IMD models is found at 46.1 and 74.0 nm. At 83.0 nm the measurement is two decades from the nearest model value (IMD). The transmission values measured at (30.4, 58.4) nm are $(0.235, 4.72 \times 10^{-3})$.

At wavelengths longer than ∼80 nm, the theoretical transmission of the Al/C filter drops steeply, from $\sim 10^{-3}$ to $\sim 10^{-9}$ between 80 and 90 nm, and a less steep decrease continues through at least 122 nm. Earth H Lyman-α dayglow is a major background source for EUV-He, but as previously noted in the literature,[3] measurement of strongly-attenuated 121.6 nm transmission is difficult in the laboratory. The theoretically-expected (model) Al/C transmission at 121.6 nm is below about 10^{-13} (Fig. 4). Accurate measurement of such small transmissions is difficult with our equipment and method, because of negligible photon count rates in the filtered portion of the lab images. For an unfiltered signal count rate of 10^4 s^{-1} (the maximum input rate of our detector system), the theoretical transmission of 10^{-13} requires an integration time of $\sim 10^9$ s (32 years) to accumulate one count. To collect counts for exposure times of 60 s–300 s (Table 2) means a measurable transmission lower limit between 3×10^{-7} and 2×10^{-5}. Based on the theoretically-predicted value of $\sim 10^{-13}$, the filter transmission at 121.6 nm (H Lyman-α) was almost certainly far below our measurement limit. Our measured value of $\sim 3 \times 10^{-7}$ should therefore be considered an upper-limit estimate to the actual transmission at 121.6 nm. The upper-limit nature of this measurement is indicated by the downward-pointing arrow (Figure 4).

4.2 Indium Filter Transmission

The measured In transmission values are listed in Table 3 and plotted in Figure 5, along with two theoretical transmission curves.[14,28,29] The solid curve gives the Henke-model[14] transmission

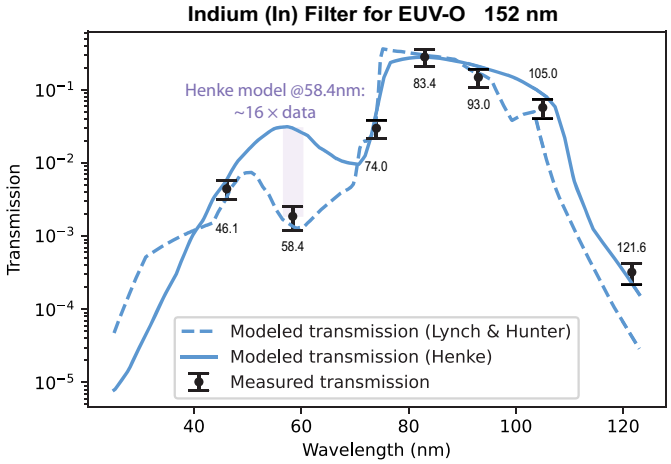

Fig. 5 EUV-O filter transmission. Measured In filter transmission, compared to modeled transmission using two different sets of optical constants. Note: bandpass purity is ≤1.3 nm (based on monochromator dispersion; cf. Sec. 3). Horizontal extent of error bars in plot is graphically arbitrary.

based on atomic form factors. These atomic form factors were derived from experimentally-determined photoabsorption cross sections where data were available, but relied on theoretical interpolations elsewhere, including at EUV wavelengths shorter than 68 nm. However, optical constants based on lab measurements of indium films are also available in compilations[28,29] that incorporate measured values of extinction coefficient (k) in the 41 to 77 nm range from earlier work.[30] The dashed curve in Fig. 5 shows the "Lynch & Hunter" (or "LH") model, using these compilation optical constants.

As with the results for Al/C, the measured In transmission values generally follow the shape of one or the other of the model curves, although (again) no single model is consistent (within errors) with all of the data points. The measurements at 46.1 and 83.4 nm each agree well (within one error bar) with both models (Henke and LH). At 74.0 and 93.0 nm, the measurements agree (within one error bar) with the LH model, but not the Henke model. The measured value at 121.6 nm agrees with the Henke model, but not the LH model. At 105.0 nm the disagreement is slightly worse for both models; ∼2 error bars below the Henke model, and a factor of three above the LH model. At 58.4 nm, the measured value of 1.9×10^{-3} is a factor of ∼16 lower than predicted by the Henke model, but agrees well with the LH model using the compilation optical constants. For the EUV-O imager, this measured 58.4 nm transmission represents significantly improved rejection of a major source of background light from neutral He.

5 Discussion

5.1 Background Rejection

To determine whether the measured filter transmissions provide the required background rejection for the EUV-He and EUV-O imagers, in Table 4, we repeated the instrument sensitivity calculation of Table 1, replacing the theoretical filter transmissions with the measured values. For each wavelength, we calculated a minimum and maximum sensitivity based on the estimated transmission uncertainties. Sensitivity estimates were used to calculate minimum and maximum rejection ratios of light at 58.4 and 121.6 nm relative to the transmission at the target wavelength of the imager [(30.4, 83.4) nm for (EUV-He, EUV-O)].

The results of the calculation are listed in Table 4. The Al/C filter achieves the required background rejection ratios at both 58.4 and 121.6 nm. The indium filters we measured were half the estimated required thickness for EUV-O, with the intention of using two filters separated by a small gap to mitigate the risk of pinholes in flight (cf. Sec. 2). Table 4 includes imager sensitivity estimates using both the measured 152 nm transmission, and the estimated transmission of an In filter 278 nm thick. Note that 278 nm is identified in Sec. 5.2 as the refined (measurement-based) estimate of OFT for EUV-O. Here, transmission is calculated to vary with thickness b as

Table 4 Estimated sensitivity of EUV-He (30.4 nm) and EUV-O (83.4 nm), based on measured transmission values.

Imager rilter	Wavelength λ (nm)	Filter transmission (%)	Sensitivity $(\mathrm{R\,s\,pix})^{-1}$	Estimated BG rejection $S_\lambda \div S_{\mathrm{target}}$	Required BG rejection
EUV-He Al (244 nm) + C (29 nm)	30.4	23.5 ± 5.2	2.21 ± 0.49	—	—
	58.4	0.47 ± 0.14	$(9.1 \pm 2.7) \times 10^{-4}$	2×10^{-4} to 7×10^{-4}	4×10^{-3}
	121.6	$\leq 2.7 \times 10^{-5}$	$\leq 2.0 \times 10^{-8}$	$\leq 1 \times 10^{-8}$	7×10^{-6}
EUV-O In (152 nm)	83.4	28.2 ± 7.5	0.91 ± 0.24	—	—
	58.4	0.19 ± 0.07	$(1.1 \pm 0.4) \times 10^{-4}$	6×10^{-5} to 2×10^{-4}	1×10^{-3}
	121.6	$(3.2 \pm 1.1) \times 10^{-2}$	$(2.3 \pm 0.8) \times 10^{-4}$	1×10^{-4} to 5×10^{-4}	1×10^{-6}
EUV-O In (278 nm[a])	83.4	9.8 ± 2.6	0.32 ± 0.08	—	—
	58.4	$(1.0 \pm 0.4) \times 10^{-3}$	$(5.9 \pm 2.2) \times 10^{-7}$	9×10^{-7} to 3×10^{-6}	1×10^{-3}
	121.6	$(3.9 \pm 1.3) \times 10^{-5}$	$(2.8 \pm 1.0) \times 10^{-7}$	5×10^{-7} to 9×10^{-7}	1×10^{-6}

[a]Estimated as $\tau = (\tau_0)^n$ with $n \equiv (b/b_0)$; cf. text.

$$\tau = (\tau_0)^n, \tag{2}$$

where $n \equiv (b/b_0)$ and τ_0 is the known transmission at thickness b_0. The 152 nm filter achieves the required 58.4 nm rejection, but not the required 121.6 nm rejection. The 278 nm filter meets or exceeds both rejection requirements.

5.2 Optimization of Filter Thicknesses

Figure 6 plots estimates of signal-to-background ratio (SBR) versus filter thickness, for the EUV-He [Fig. 5(a)] and EUV-O [Fig. 5(b)] imagers. SBR is calculated from expected counts, as follows. The per-pixel count rate [in $(\mathrm{s\,pixel})^{-1}$] is computed as the product of sensitivity S_λ [cf. Eq. (1), in $(\mathrm{R\,s\,pixel})^{-1}$] and expected brightness (B). The SBR is then the ratio of signal counts to background counts. Minimum and maximum values of SBR are defined as

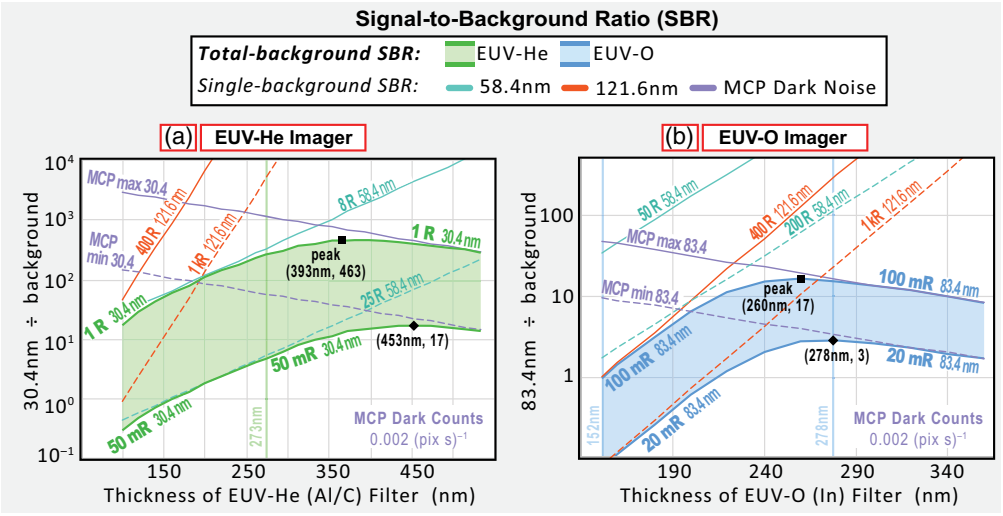

Fig. 6 Optimization of filter thickness: SBR for (a) EUV-He and (b) EUV-O imagers. In each plot, shaded region shows expected range of the ratio of signal (30.4 or 83.4 nm) to total background count rates. Peaks indicate optimum filter thickness. Diagonal lines plot SBR for individual background sources (58.4 nm, 121.6 nm, and MCP dark counts).

$$\mathrm{SBR}_{\mathrm{min}} = (\text{signal counts})_{\mathrm{min}} \div (\text{back ground counts})_{\mathrm{max}}, \quad (3)$$

$$\mathrm{SBR}_{\mathrm{max}} = (\text{signal counts})_{\mathrm{max}} \div (\text{back ground counts})_{\mathrm{min}}. \quad (4)$$

In Fig. 6, diagonal lines are SBRs for individual background sources (58.4 nm, 121.6 nm, and MCP dark counts); for each background source, (minimum, maximum) values are plotted as (dashed, solid) lines. Each line is labeled with its corresponding background B value. For example, the dashed red line labeled "1 kR" in Fig. 6(a) gives the ratio of 30.4 nm minimum-signal ($B_{30.4\ \mathrm{nm}} = 50$ mR; see below) counts to 121.6 nm maximum-background ($B_{121.6\ \mathrm{nm}} = 1$ kR) counts. For MCP dark-noise background, the two diagonal lines (dashed and solid) share the same dark rate [0.002 $(\mathrm{s\,pixel})^{-1}$], per the G18 estimate,[6] and differ only by the signal brightness (minimum or maximum).

The overall instrument SBR (including all background sources) is given by the shaded region in each plot. The (lower, upper) edges of the shaded region are the (minimum, maximum) SBR for the range of expected signal brightness: (50 mR, 1 R) for 30.4 nm, and (20 mR, 100 mR) for 83.4 nm.[3,6] For example, the lower edge labeled "20 mR" in Fig. 6(b) gives the ratio of 83.4 nm minimum-signal ($B_{83.4\ \mathrm{nm}} = 20$ mR) counts to total (from 58.4 nm, 121.6 nm, and MCP dark noise) maximum-background counts.

The overall SBR (shaded region) in each plot results from the interplay of external-light background versus internal (MCP) background. As the filter gets thicker, $\mathrm{SBR}_{58.4\ \mathrm{nm}}$ and $\mathrm{SBR}_{121.6\ \mathrm{nm}}$ increase because the filter attenuates the background more than the signal. But as the filter thickens, $\mathrm{SBR}_{\mathrm{MCP}}$ decreases because the filter attenuates the signal but does not affect the dark noise. Thus, each overall SBR plot contains a broad peak where the filter thickness is optimized. Peak SBR performance lies in the range ~390 to 450 nm for EUV-He, and ~260 to 280 nm for EUV-O. For reference, the filter thickness values from Table 4 are indicated in the figure for both imagers. Recall that for EUV-O, in Sec. 2 the initial OFT estimate of 303 nm was obtained from model-derived transmission values. Based on our laboratory measurements of indium filter transmission, that initial OFT estimate is here refined. Along the 20 mR (worst-case) curve, the peak SBR, for which the background rejection requirement ($\leq 10^{-6}$) is exceeded (Table 4), occurs at filter thickness 278 nm [Fig. 6(b)].

To the left of the total SBR peak (where the slope is positive) in each plot, the curve asymptotically follows the dominant single-source background diagonal. In Fig. 6(a), the EUV-He curve in the thickness range 150 to 250 nm follows the $\mathrm{SBR}_{58.4\ \mathrm{nm}}$ diagonal because the Al/C filter is more effective at reducing 121.6 nm than 58.4 nm. In Fig. 6(b), the EUV-O curve for thickness <190 nm follows the $\mathrm{SBR}_{121.6\ \mathrm{nm}}$ diagonal because the In filter attenuation is comparable for 58.4 and 121.6 nm, and the latter background is brighter. Thus, the respective (EUV-He, EUV-O) filter designs are driven by (58.4, 121.6) nm. EUV-He SBR is ample for a broad range of Al/C filter thicknesses; EUV-O SBR is adequate for a much narrower range of In filter thicknesses. Because this EUV-O performance is dominated by the 121.6 nm background, future work should attempt to improve 121.6 nm rejection. Alternately, EUV-O imaging would benefit from simultaneous Lyman-α background imaging, so the large 121.6 nm background can be subtracted.

Table 5 computes EUV-He and EUV-O count rates and cadences, using measurement-derived transmissions of Al (244 nm) + C (29.2 nm) and In (278 nm) filters. Estimates are provided for three signal values the minimum, the maximum, and the geometric mean of the

Table 5 Count rates and cadences of EUV-He (30.4 nm) and EUV-O (83.4 nm) imagers, using measurement-derived transmissions of Al (244 nm) + C (29.2 nm) and In (278 nm) filters.

			Signal (R)			Count Rate $(\mathrm{s\,pix})^{-1}$			Cadence		
Imager	Filter transmission	Sensitivity $(\mathrm{R\,s\,pix})^{-1}$	Min	Max	geom mean	Min	Max	geom mean	slowest	fastest	geom mean
EUV-He 30.4 nm	0.235	2.21	0.05	1.0	0.224	0.111	2.212	0.495	90 s	5 s	20 s
EUV-O 83.4 nm	0.098	0.32	0.02	0.1	0.045	0.006	0.032	0.014	26 min	5 min	12 min

maximum and minimum. For this computation, each 2D pixel has solid angle $(0.45\ \text{deg})^2$, i.e., the same as a resolution element (Sec. 2). The count rate is the per-pixel sensitivity times the signal. Following previous work,[6] cadence values assume a requirement of 10 counts per pixel, per exposure; i.e., 32% counting error. EUV-He count rates of 0.1 to 2.2 $(\text{s pixel})^{-1}$ are sufficient for 5 to 90 s time resolution. EUV-O's much lower count rates of 0.006 to 0.032 $(\text{s pixel})^{-1}$ result from both lower sensitivity and a much weaker expected signal range. EUV-O count rates are sufficient for a much slower 5 to 26 min cadence. Clearly, imaging the dense oxygen torus is more challenging than imaging the helium plasmasphere.[6]

6 Conclusions

We presented measurements of EUV transmission for two thin film filters designed to obtain improved EUV-He images of plasmaspheric He^+, and the first global EUV-O images of O^+/O^{++} in the dense oxygen torus. We find that the measured filter performance meets or exceeds background rejection requirements for both imagers, EUV-He and EUV-O. Compared to previous He^+30.4 nm imaging that used an Al filter, we find that a combined Al/C filter achieves superior rejection of 58.4 nm background from neutral He. We also find that an In filter provides the required 83.4 nm transmission and adequate rejection of brighter 58.4 and 121.6 nm background light. The measured In transmission at 58.4 nm is a factor of ~16 lower than predicted based on optical constants that rely on interpolations at $\lambda < 68$ nm. For the EUV-O imager, this measured 58.4 nm transmission represents significantly improved rejection of a major source of background light from neutral He. Because this EUV-O performance is dominated by the 121.6 nm background, future work should attempt to improve 121.6 nm rejection. Alternately, EUV-O imaging would benefit from simultaneous/companion Lyman-α background imaging, so this large background can be subtracted.

Code and Data Availability

All data in support of the findings of this paper are available within the article, in Tables 1, 3, and 4. The IMD software used to model filter transmission is available at the Reflective X-ray Optics website (http://www.rxollc.com/idl/index.html).

Acknowledgments

This work was supported by funding from Southwest Research Institute Internal Research Project 15-R8322, and NASA Grant 80NSSC18K1244 via the Heliophysics Technology and Instrument Development for Science (H-TIDeS) program.

References

1. J. Goldstein, "Plasmasphere response: tutorial and review of recent imaging results," *Space Sci. Rev.* **124**, 203–216 (2006).
2. J. Goldstein et al., "The Future of Plasmaspheric Extreme Ultraviolet (EUV) imaging," in *Magnetospheric Imaging*, Y. Colado-Vega et al., Eds., Chapter 6, pp. 231–286, Elsevier (2022).
3. B. R. Sandel et al., "The extreme ultraviolet imager investigation for the IMAGE mission," *Space Sci. Rev.* **91**, 197–242 (2000).
4. M. W. Davis et al., "An improved wide-field camera for imaging Earth's plasmasphere at 30.4 nm," *Proc. SPIE* **8859**, 88590U (2013).
5. P. W. Vedder et al., "Filters for the EUV Explorer: calibration and lifetesting results," *Proc. SPIE* **1159**, 392 (1989).
6. J. Goldstein et al., "Imaging the global distribution of plasmaspheric oxygen," *J. Geophys. Res.* **123**, 2078–2103 (2018).
7. B. J. Fraser et al., "The relationship between plasma density structure and EMIC waves at geosynchronous orbit," in *Inner Magnetosphere Interactions: New Perspectives from Imaging*, J. L. Burch, M. Schulz, and H. Spence, Eds., p. 55, American Geophysical Union, Washington, DC (2005).
8. J. L. Horwitz, R. H. Comfort, and C. R. Chappell, "Thermal ion composition measurements of the formation of the new outer plasmasphere and double plasmapause during storm recovery phase," *Geophys. Res. Lett.* **11**, 701–704 (1984).
9. M. Nosé et al., "Oxygen torus in the deep inner magnetosphere and its contribution to recurrent process of O^+-rich ring current formation," *J. Geophys. Res.* **116**, A10224 (2011).

10. W. T. Roberts, Jr. et al., "Heavy ion density enhancements in the outer plasmasphere," *J. Geophys. Res.* **92**, 13499–13512 (1987).
11. W. C. Walker, O. P. Rustgi, and G. L. Weissler, "Optical and photoelectric properties of thin metallic films in the vacuum ultraviolet," *J. Opt. Soc. Am.* **49**, 471–475 (1959).
12. W. R. Hunter, D. W. Angel, and R. Tousey, "Thin films and their uses for the extreme ultraviolet," *Appl. Opt.* **4**, 891–898 (1965).
13. R. Henneck, K. Bjoerknaes, and S. R. Jelinsky, "Transmission of thin indium filters in the EUV and lifetime tests," *Proc. SPIE* **3114**, 648–651 (1997).
14. B. L. Henke, E. M. Gullikson, and J. C. Davis, "X-ray interactions: photoabsorption, scattering, transmission, and reflection at $E = 50 - 30{,}000$ eV, $Z = 1 - 92$," *At. Data Nucl. Data Tables* **54**, 181–342 (1993).
15. A. Yamazaki et al., "Development of instrument for the resonance scattering emission of oxygen ion (OII:83.4 nm): toward the imagery of magnetosphere," *J. Commun. Res. Lab.* **49**(4), 107–120 (2002).
16. M. W. Davis et al., "Radiometric performance results of the Juno ultraviolet spectrograph (Juno-UVS)," *Proc. SPIE* **8146**, 814604 (2011).
17. C. D. Ertley et al., "Microchannel plate imaging detectors for high dynamic range applications," *IEEE Trans. Nucl. Sci.* **64**, 1774–1780 (2017).
18. E. L. Christian and J. H. Kerr, "Ballistic limit equations for spacecraft shielding," *Int. J. Impact Eng.* **26**, 93–104 (2001).
19. R. B. Hoover et al., "Performance of compact multilayer coated telescopes at soft X-ray/EUV and far ultraviolet wavelengths," *Opt. Eng.* **29**, 1281 (1990).
20. M. W. Davis et al., "Improved ground calibration results from Southwest Research Institute Ultraviolet Radiometric Calibration Facility (UV-RCF)," *Proc. SPIE* **9144**, 914433 (2014).
21. K. Danzmann et al., "High current hollow cathode as a radiometric transfer standard source for the extreme vacuum ultraviolet," *Appl. Opt.* **27**, 004947 (1988).
22. I. Kanik, J. M. Ajello, and G. K. James, "Extreme ultraviolet emission spectrum of CO2 induced by electron impact at 200 eV," *Chem. Phys. Lett.* **211**, 523–528 (1993).
23. R. Mills and P. Ray, "Extreme ultraviolet spectroscopy of helium hydrogen plasma," *J. Phys. D Appl. Phys.* **36**, 1535 (2003).
24. A. Kramida et al., "Nist atomic spectra database (ver. 5.9)," National Institute of Standards and Technology, Gaithersburg, MD (2021). https://physics.nist.gov/asd (accessed 8 April 2022).
25. Y. Ralchenko and A. Kramida, "Development of NIST atomic databases and online tools," *Atoms* **8**(3), 56 (2020).
26. B. M. Lairson et al., "Improved EUV filter transmission with plasma cleaning," *Proc. SPIE* **7732**, 77322G (2010).
27. D. L. Windt, "IMD: software for modeling the optical properties of multilayer films," *Comput. Phys.* **12**, 360–370 (1998).
28. D. W. Lynch and W. R. Hunter, "Introduction to the data for several metals," in *Handbook of Optical Constants of Solids*, E. D. Palik, Ed., p. 233, Academic Press, Burlington (1997).
29. D. W. Lynch and W. R. Hunter, "An introduction to the data for several metals," in *Handbook of Optical Constants of Solids*, E. D. Palik, Ed., p. 341, Elsevier (1998).
30. G. Jezequel et al., "Optical transitions from d core states in polycristalline indium, tin and lead," *Solid State Commun.* **23**(8), 559–562 (1977).

Todd Veach is an astrophysicist, specializing in the design, fabrication, and operation of laboratory, ground-based, balloon-borne, and spaceflight astronomical instruments. His research interests include UV/vis/IR imaging and spectroscopy, FIR interferometry, cryogenics, astronomical detector development, star formation, supernovae, extra-solar planet formation and evolution, and cosmological structure formation. He has more than 15 years of experience with UV/vis/IR imaging and spectroscopy, FIR interferometry, cryogenics, astronomical detector development, calibration, and cryogenic system design.

Michael Davis is an astrophysicist, specializing in designing and testing astronomical instruments. His research interests include UV/vis/IR instrumentation, planetary atmospheres, and galactic astrophysics. He has integrated and tested UV instrumentation for more than 20 years, including the ALICE spectrograph for New Horizons, the LAMP spectrograph for LRO, and the UVS instruments for the Juno, JUICE, and Europa Clipper missions. He has authored or co-authored more than 70 technical papers in ultraviolet spectroscopy and astronomical instrumentation.

Jerry Goldstein is a space physicist who specializes in the dynamics of inner magnetospheres using global imaging observations from extreme ultraviolet (EUV) and energetic neutral atom

(ENA) camera, complemented by theory and simulation. He develops EUV and ENA cameras for improved imaging of the terrestrial plasmasphere, and Jupiter's Io plasma torus. He has decades of experience with data analysis and modeling of plasma dynamics in geospace and in outer planet magnetospheres.

Biographies of the other authors are not available.